energies

MDPI

Article

Enhanced Power Quality in Single-Phase Grid-Connected Photovoltaic Systems: An Experimental Study

Abdellah Benabdelkader [1], Azeddine Draou [2], Abdulrahman AlKassem [2], Toufik Toumi [1], Mouloud Denai [3], Othmane Abdelkhalek [1] and Marwa Ben Slimene [4,5,*]

[1] Smart Grids & Renewable Energies Laboratory, Faculty of Technology, University of Tahri Mohammed Bechar, Bechar 08000, Algeria
[2] Department of Electrical Engineering, College of Engineering, Islamic University in Madinah, Madinah 42351, Saudi Arabia
[3] School of Physics, Engineering & Computer Science, University of Hertfordshire, Hatfield AL10 9AB, UK
[4] Department of Computer Science and Engineering, College of Computer Science and Engineering, University of Ha'il, Ha'il 55436, Saudi Arabia
[5] SIME Laboratory, ENSIT, University of Tunis, 05 Ave Taha Hussein, Tunis 1008, Tunisia
* Correspondence: benslimene.marwa@gmail.com

Abstract: The main aim of the research work presented in this paper consists of proposing an effective control scheme for a grid-connected single-phase photovoltaic (PV) system to enhance not only the power quality at the point of common coupling (PCC) but also to operate with a maximum power point tracking (MPPT) controller. Moreover, an orthogonal signal generator (OSG) module for effective grid synchronization, a current reference generation controller, and a PWM generating block have also been designed and included in this paper. The proposed control strategy allows the MPPT controller to switch to faulty mode and maintains the voltage according to network requirements using an adaptive neuro-fuzzy inference system (ANFIS)-based control whenever a fault occurs at the PCC. The performance of the analyzed control strategy, which is based on the static compensation of the DC-link voltage fluctuations in a grid-connected inverter powered by PV, is further explored through simulations in MATLAB, and the results are included in this paper. Moreover, the control scheme is implemented experimentally using a dSPACE DS 1104 control board and then assessed on a small laboratory-scale single-phase PV system that is subjected to some fault scenarios. The simulation and experimental results have shown improved power quality and robustness against grid fluctuations, resulting in better dynamic performance.

Keywords: photovoltaic; orthogonal signal generator; ANFIS; MPPT; DC-AC power quality

Citation: Benabdelkader, A.; Draou, A.; AlKassem, A.; Toumi, T.; Denai, M.; Abdelkhalek, O.; Ben Slimene, M. Enhanced Power Quality in Single-Phase Grid-Connected Photovoltaic Systems: An Experimental Study. *Energies* **2023**, *16*, 4240. https://doi.org/10.3390/en16104240

Academic Editor: Daniela Cristina MOMETE

Received: 8 April 2023
Revised: 5 May 2023
Accepted: 9 May 2023
Published: 22 May 2023

1. Introduction

In recent years, power quality (PQ) has become a real problem for both utility providers and consumers due to the widespread interconnection of power-electronic-based nonlinear loads to the electricity distribution grid. Voltage sags and swells are among the most common PQ issues affecting consumers' critical loads [1–4]. A voltage sag is defined as a drop in the AC voltage's RMS value at a power frequency of 0.5 cycles per minute, according to IEEE 1346 [5] and IEEE 1159 [5–7] standards. It can also be defined as a rapid drop and simultaneous fast recovery in the voltage at any point of the electrical system according to the standard IEC 61000-2-1 [8]. Voltage sags are often caused by short-circuit faults such as single line-to-ground faults due to the sudden interconnection of a large load such as an industrial induction motor. A voltage swell is described by the IEEE standards as a rise in the RMS value of the supply voltage from 1.1 p.u. to 1.8 p.u. of the nominal voltage during a period from 0.5 s to one minute. The interconnection of large capacitors or the disconnection of large loads are the two primary sources of voltage surges. As a result, some of the industrial equipment, such as motor drives, surge arresters, and relays, may be

overheated, tripped, or even damaged by voltage surges [8,9], whereas, for sensitive loads such as electronic equipment, harmonic pollution is of major concern because its regulation is based on the crossings of the zero or maximum value point of the supply voltage [3–7].

Renewable energy generation technology based on power electronics is developing rapidly. New energy generation technology is based on photovoltaic (PV) systems, which are generally located in mountainous areas and deserts to receive more sunlight. In addition, these remote areas are conducive to the large-scale installation of PV inverters [10,11]. Recently, an increase in the deployment of solar PV systems, from rooftop installations to large-scale solar farms in the megawatt range, has been driven not only by the continuous fall in the price of PV modules but also by the consumers' rising awareness of and wish to adopt eco-friendly energy solutions [9]. Future PV systems are expected to meet power generation needs from a point closer to the point of consumption [12–14] to avoid transmission losses and enhance the efficiency of the distribution network. Although there is an extensive body of literature on PV systems, this area is still an active area of ongoing research and development. Solar energy plays a leading role in reducing greenhouse gas emissions and has received strong support through various incentive programs, although the price is still expensive.

In previous research [15,16], the authors describe a modeling technique and fuzzy logic-based MPPT controller for efficient maximum power extraction. The authors of [17] presented an accurate method to adjust the duty cycle under different climatic conditions. The switching pulses of the power converter semiconductor devices, which regulate the active and reactive forms of power, are generated using a peak current controller [18–20]. Future PV systems should be capable of managing reactive power, islanding detection, power quality enhancement, and fault ride-through (FRT), as described in earlier studies [21–23]. In grid-connected inverter systems, some of the voltage amplitudes and frequencies are fundamentally critical parameters; accurate knowledge of these parameters is vital for obtaining the appropriate reference signals and meeting the requirements of future grids [24,25].

In another study [26], the authors have shown that power electronic equipment consumes large quantities of reactive power and can lead to the introduction of harmonics into the network. The authors of [27] have proposed a conventional PI controller to enhance the power quality of a multilayer single-phase inverter. The authors of [28,29] have stressed that voltage sag is a frequent problem that often results in unnecessary tripping when applied to a single-phase system operating in both ON and OFF grid modes. In addition, in an earlier study [30], the authors use a PV system to solve a problem related to the efficient control of the reactive power caused by using loads that influence the current supplied from the source. In islanded mode, the voltage controller maintains the sinusoidal waveforms of the load voltage. In various other studies [31–33], the authors stated that the synchronization controller ensures the transition between the bidirectional islanded and grid-connected modes, depending on the grid's accessibility.

The work presented in this paper intends to carry out experimental analysis on a laboratory prototype to assess the dynamic performance of single-phase grid-connected PV systems that are subjected to various faults. One of the merits of this research is to implement a PV system controller to regulate the active and reactive powers required by the load. A perturb and observe (P&O) and maximum power point tracking (MPPT) algorithm is introduced to allow the PV system to operate at its maximum power. In addition, when a fault occurs at the point of common coupling (PCC) under any voltage sag circumstances, the controller will inject a reactive current, and the system may operate in islanded mode.

The rest of the paper is organized as follows. Section 2 gives a description of the proposed system considered in this work. Section 3 describes the power control concepts and Section 4 presents the proposed ANFIS-based power controller. Section 5 is devoted to the various grid synchronization techniques. In Section 6, a series of simulation results are inserted, and in Section 7, the hardware test bed of the grid-connected PV system developed in this paper is described, together with the introduction of a series of experimental test results. Finally, Section 8 summarizes the main conclusions of the paper.

2. Description of the System

For PV systems to operate effectively, it is necessary to control various parameters, such as the PV side for maximum power extraction, the inverter side for injecting high-quality current, and the grid side for any additional tasks. The ambient temperature and solar irradiance must be considered during a PV system's design and planning phases. These factors greatly influence the PV system's output power [34,35]. Figure 1 shows the schematic diagram of a system comprising a dual stage with a PV system connected to the PCC through a DC-DC boost converter, grid inverter, and control system as proposed in the literature [7,22]. The system may operate in both grid-connected and islanded modes.

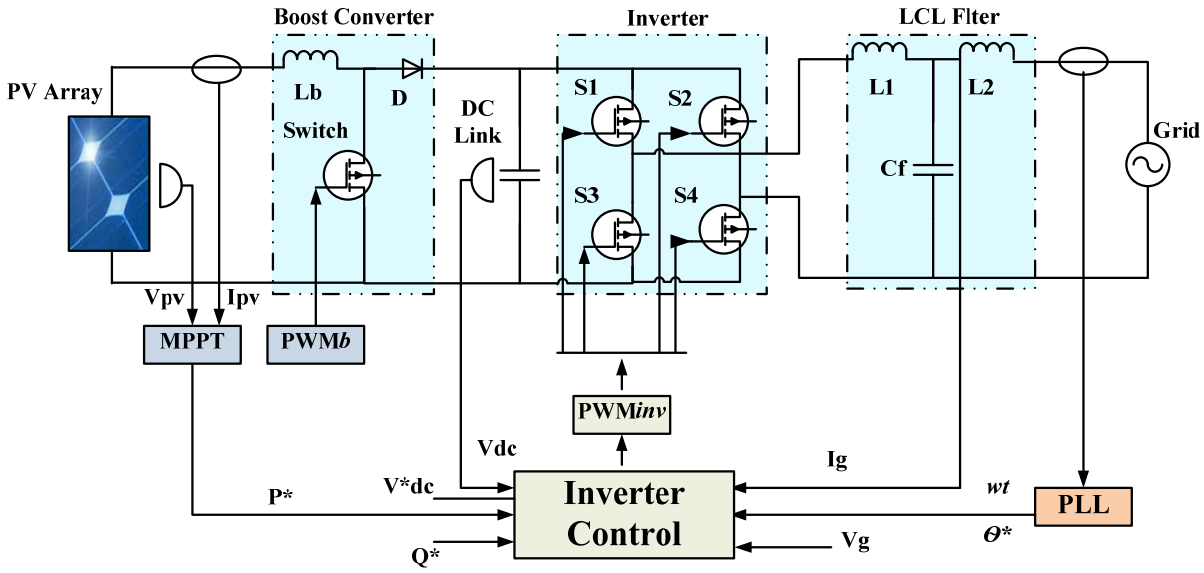

Figure 1. Schematic diagram of the grid-connected PV system.

3. PV Array Modeling

The PV cell is the basic unit of a PV module; it transforms the photons of the sun's rays directly into electric power. Figure 2 shows the equivalent circuit of a PV system, which consists of N strings of PV modules in parallel with a line consisting of series M modules to achieve the appropriate power rating.

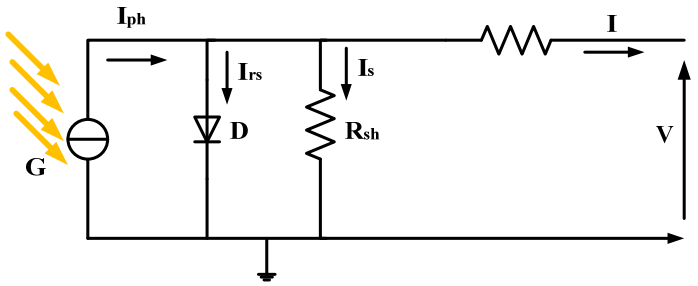

Figure 2. Equivalent circuit of a PV cell.

The dynamic model of the PV array is described by the following equations [36].

$$I = N_p I_{ph} - N_p I_0 \left[\exp\left(\frac{q(V_{pv} + I_{pv} R_{sh})}{N_s AKT} \right) - 1 \right] - \frac{V + IR_{sh}}{R_{sh}} \quad (1)$$

$$I_s = I_{rs} \left(\frac{T_c}{T_{ref}} \right)^3 \left[\exp\left(\frac{qE_g \left(\frac{1}{T_{ref}} - \frac{1}{T_c} \right)}{KA} \right) \right] \quad (2)$$

$$I_{rs} = \frac{I_s}{\left[\exp\left(\frac{qV_{oc}}{N_s KAT}\right) - 1\right]} \quad (3)$$

$$I_{ph} = [K_i(T - T_{ref})]\left(\frac{G}{1000}\right) \quad (4)$$

To be able to produce maximum power, the PV module must work within a peak value P_{max} of the output power. The MPPT algorithm used in this study is based on the well-known P&O technique, and a 1 kW PV system is considered.

4. Analysis of Power Control

This section discusses the control scheme of a single-stage single-phase grid-connected PV system. In normal cases, the PV solar system would be operated in MPPT mode, which may give maximum power to the grid. However, when a fault occurs at the PCC, the grid will require the PV inverter to supply a reactive current to boost it [7]. During islanding, this mode will switch to fault mode, as illustrated by the flowchart diagram in Figure 3.

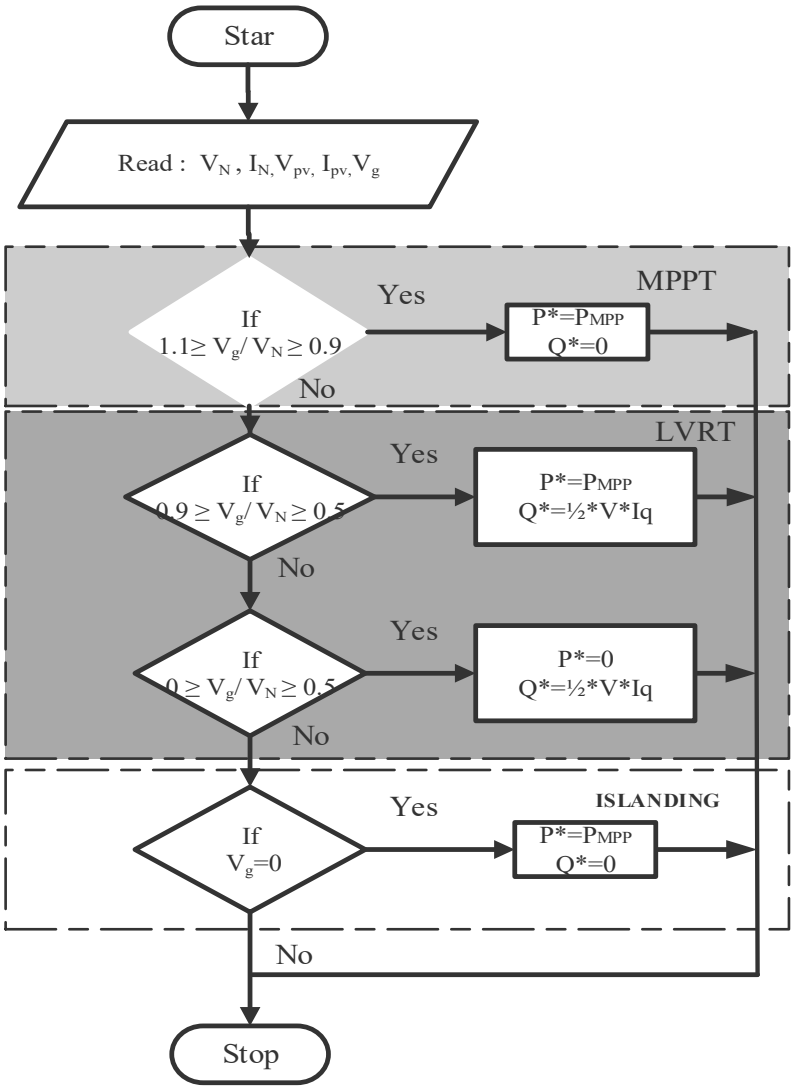

Figure 3. Flowchart describing the generation of the reference powers.

The control block diagram of the PV system is shown in Figure 4. It consists of the MPPT, the orthogonal signal generator (OSG) unit, the PWM block, and the PI controllers

for current reference generation. A low pass (LP) filter is introduced to smooth the inverter output voltage waveform. In the EF frame, the grid current and voltage components are represented by I_{gE}, I_{gF}, and V_{gE}, V_{gF}, respectively. The real (P) and reactive (Q) powers are defined by the following equations [23] and their values may be calculated using OSG systems in the same manner as in the dq-rotating reference frame:

$$P = \frac{1}{2}\left(V_{g\alpha}\ \ I_{g\alpha} + I_{g\beta}\ \ V_{g\beta}\right) \tag{5}$$

$$Q = \frac{1}{2}\left(V_{g\alpha}\ \ I_{g\alpha} - I_{g\beta}\ \ V_{g\beta}\right) \tag{6}$$

in which the currents in the $\alpha\beta$-stationary reference frame are given by:

$$\begin{bmatrix} i_{g\alpha} \\ i_{g\beta} \end{bmatrix} = \frac{2}{v_{g\beta}^2 + v_{g\beta}^2} \begin{bmatrix} v_{g\alpha} & v_{g\beta} \\ v_{g\beta} & -v_{g\alpha} \end{bmatrix} \begin{bmatrix} P \\ Q \end{bmatrix}. \tag{7}$$

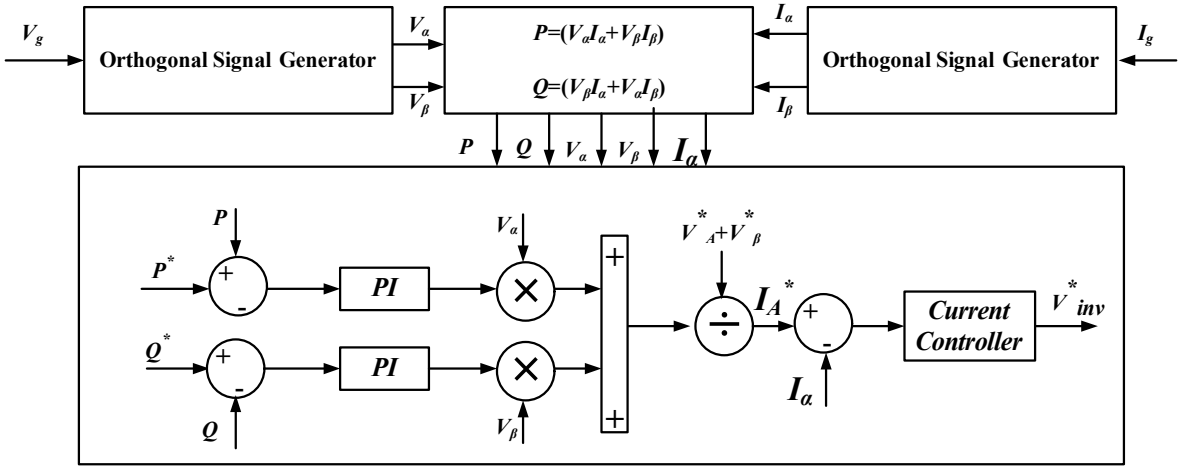

Figure 4. Proposed control block diagram of the system based on PQ theory and the OSG concept.

A controller such as a PI may be used to regulate the power since both powers are constant current quantities. The current reference is given by:

$$\begin{bmatrix} i_{g\alpha}^* \\ i_{g\beta}^* \end{bmatrix} = \frac{2}{v_{g\beta}^2 + v_{g\beta}^2} \begin{bmatrix} v_{g\alpha} & v_{g\beta} \\ v_{g\beta} & -v_{g\alpha} \end{bmatrix} \begin{bmatrix} G_P(s)\ (P - P^*) \\ G_q(s)\ (Q - Q^*) \end{bmatrix}. \tag{8}$$

The transfer functions of the PI controllers for both these powers may be expressed as:

$$\begin{aligned} G_P(s) &= K_{pp} + K_{pi}\tfrac{1}{s} \\ G_q(s) &= K_{qp} + K_{qi}\tfrac{1}{s} \end{aligned}. \tag{9}$$

5. ANFIS-Based Controller Development

ANFIS belongs to the class of neuro-fuzzy systems, which combine the learning capability and the parallel computation of neural networks with fuzzy systems. Neuro-fuzzy systems can be trained to develop fuzzy rules and determine the membership functions for the variables of the system. The structure of a neuro-fuzzy system is similar to that of a multi-layer neural network and includes an input and an output layer, along with three hidden layers that represent the membership functions and fuzzy rules. ANFIS training uses a hybrid learning algorithm combining the least-squares estimator (forward pass) and the gradient descent method (backward pass) [37]. These features provide ANFIS with superior performance and robustness [38]. In this section, an ANFIS-based controller

is proposed for the control of the inverter DC-link voltage. Details of the design steps and a list of the parameters of the ANFIS training are given in Appendix A. Figure 5 depicts the triangular membership functions of the error, ε, and error change, $\Delta\varepsilon$. Figure 6 illustrates the variations of the output against the two inputs ε and $\Delta\varepsilon$. ANFIS was originally designed with bell-shaped MFs.

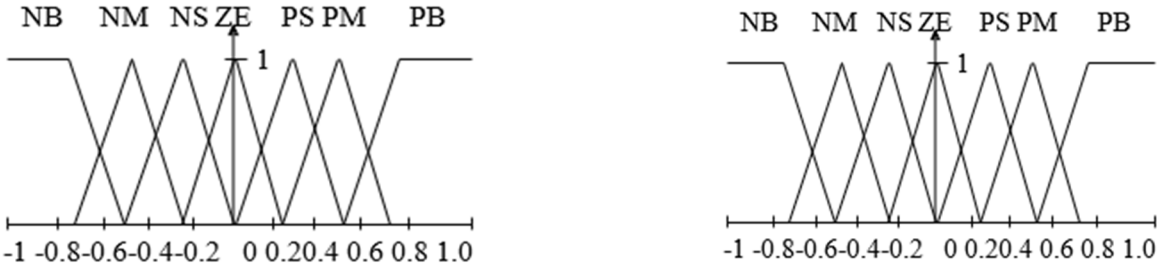

(**a**) Error (**b**) Change in error

Figure 5. Triangular membership functions.

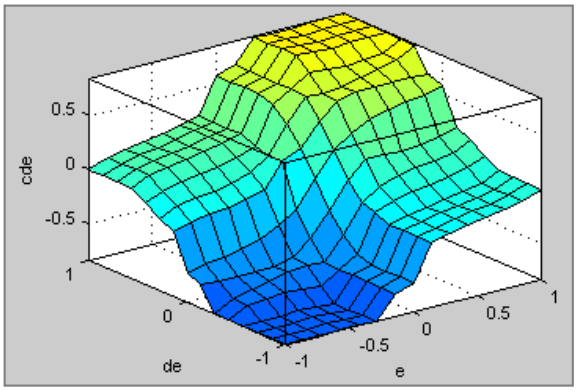

Figure 6. Surface view of the ANFIS controller.

6. Grid Synchronization Techniques

Following grid failures due to the occurrence of a fault, the synchronization of single-phase PV systems is critical. A system with good synchronization capabilities would have to be designed to respond quickly to any voltage drop. In the recent literature, several synchronization methods have been proposed [38], which may be broadly categorized into two groups:

1. Mathematical methods, e.g., synchronized Fourier- and PLL-based methods. Currently, PLL-based synchronization techniques are the most popular choices since the design of a phase detector, a simple sinusoidal multiplier [38,39]. In a single-phase system, however, this procedure will result in a double-frequency term. Another approach to removing phase error for a PLL-based method is to apply the Park transform to an OSG system. A PLL based on T/4 delay [37] and inverse Park transform-based PLL (IPT-PLL) [40] are examples of such PLLs.
2. Another approach is to employ adaptive filters that can automatically modify the output. The OSG is utilized to help in the calculations of active and reactive powers and provides appropriate grid synchronization. The OSG system is used to calculate P and Q. Figure 7 depicts the OSG for a single-phase system [7].

The reactive power is subjected to:

$$I_p^2 + I_q^2 = I_N^2 \leq I_{max}. \tag{10}$$

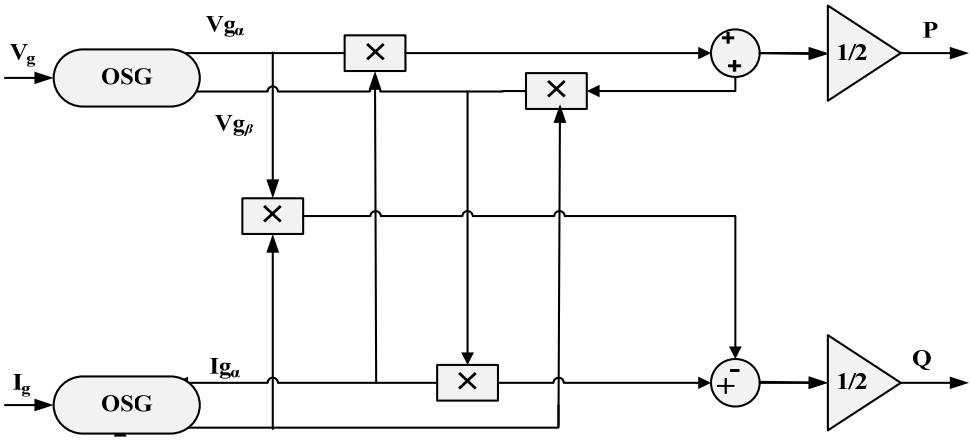

Figure 7. Orthogonal signal generation procedure.

The minimum value of the reactive current (I_q) to be injected into the grid system is given by Equation (11). The active power is controlled to keep the frequency constant.

$$I_q = \begin{cases} 0.9 \le \frac{V_g}{V_N} \le 1 \\ 2 \times \frac{V_g}{V_N} \times I_N, \; 0.5 \le \frac{V_g}{V_N} \le 0.9 \\ I_N, \qquad 0.9 \le \frac{V_g}{V_N} \le 1 \end{cases} \tag{11}$$

$$I_p = \begin{cases} Im, & 0.9 \le \frac{V_g}{V_N} \le 1 \\ \sqrt{I_N - \left(2 \times \frac{V_g}{V_N} \times I_N\right)}, & 0.5 \le \frac{V_g}{V_N} \le 0.9 \\ 0, & 0.1 \le \frac{V_g}{V_N} \le 0.5 \end{cases} \tag{12}$$

Several recent papers have dealt with control methods to suppress the injected current harmonics. In this case, the harmonic compensation method is used, as shown in Figure 8.

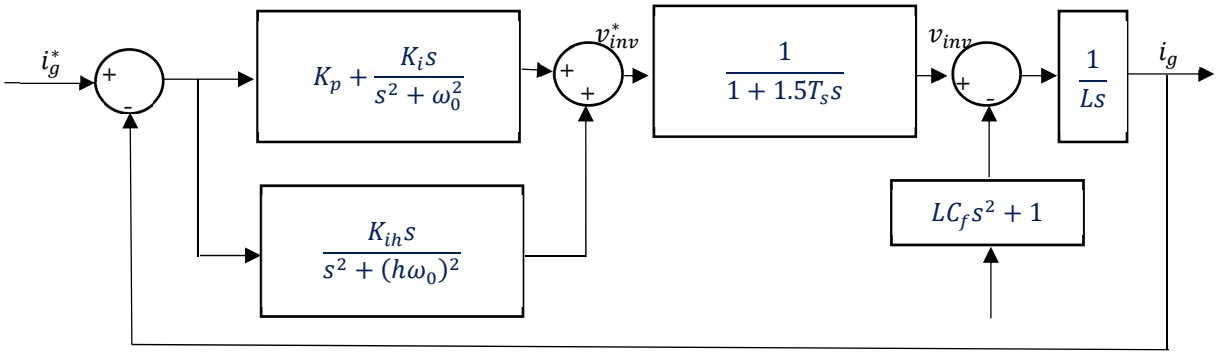

Figure 8. Block diagram of the current control loop for harmonic voltage distortion elimination.

Thus, the closed-loop transfer function is obtained as:

$$\frac{i_g(s)}{i_g^*(s)} = \frac{G_{PR+HC}(s) \;\; G_d(s)}{LS + G_{PR+HC}(s) \;\; G_d(s)} \tag{13}$$

where $G_{PR+HC}(s)$ represents the controller's transfer function and $G_d(s)$ is the processing time delay.

The relationship of $G_{PR+HC}(s)$ and $G_d(s)$ can also be written as:

$$G_{PR+HC}(s) = K_p + \frac{K_i s}{s^2+\omega_0^2} + \sum_{h=3,5,3,7\ldots} \frac{K_{ih} s}{s^2+(h\omega_0)^2}$$
$$G_d(s) = \frac{1}{1+1.5T_s s} \quad (14)$$

$$\left(G_{HC}(s) = \frac{K_{ih} s}{s^2 + (h\omega_0)^2} \right) \quad (15)$$

where k_p is the value of the proportional gain and k_{ih} represents the resonant and harmonic compensator gains, respectively; h represents the value of the harmonic order, ω_0 denotes the value of the fundamental frequency, and T_s represents the value of the sampling period.

The current control strategy will decide on the quality of the power injected into the grid and the precise harmonics compensators [7] that are required to achieve this. In the *BC* reference frame, the gains of the PR and HC controllers are defined by Equations (14) and (15) respectively.

The PV system parameters are listed in Table 1. Details of the Simulink implementation of a single-phase grid-connected PV system with an LCL filter is given in Appendix C.

Table 1. PV panel, Boost converter, and load specifications.

Component	Value
PV panel maximum power	
LC filter values	2.3 mH, 100 KF
Linear load	450 W, 125 Var
Nonlinear load	850 W, 250 Var
Converter values	2.9 mH, 70 KF, 15 kHz

7. Simulation Results

The performance of the proposed control strategy, applied to a grid-connected inverter powered by PV solar energy, has been analyzed through a simulation created using MATLAB 2016 b. The combined PV array and DC-DC boost converter is connected to the grid through a voltage source inverter. A filter is introduced to obtain a near-sinusoidal voltage waveform.

Figure 9a,b shows the various forms of power during islanding and sag voltage. Moreover, the DC link voltage and real and reactive powers' waveforms for a linear load are depicted in Figure 10a,b, respectively. These results show the good performance of the proposed control system.

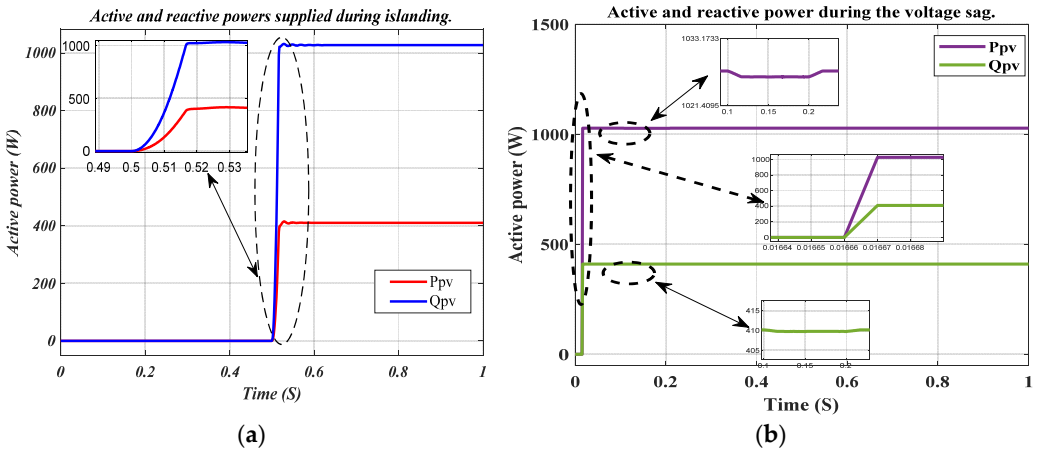

(**a**) (**b**)

Figure 9. Real and reactive power: (**a**) during islanding, (**b**) during sag voltage.

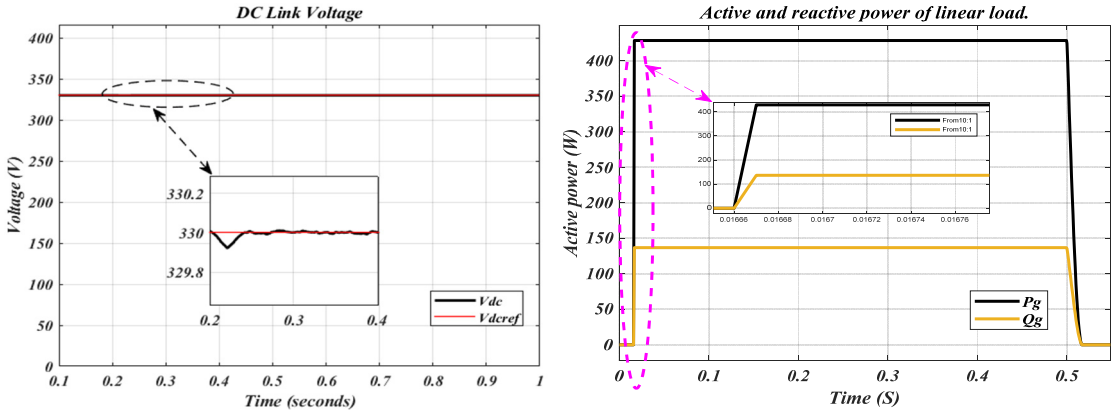

(**a**) (**b**)

Figure 10. Waveforms for a linear load of (**a**) DC link voltage, and (**b**) real and reactive power.

Figure 11a,b shows the various forms of power in the case of power supplied by the source and PV system.

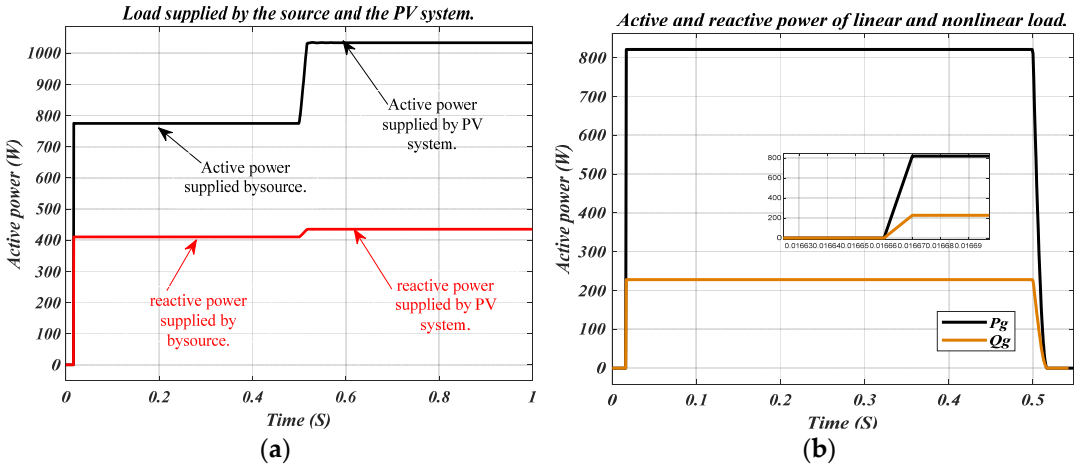

(**a**) (**b**)

Figure 11. Simulation results: (**a**) load supplied by the source and PV; (**b**) real and reactive power for linear and nonlinear loads.

The proposed system is assessed under fault conditions, in the presence of a sag applied at t = 0.1 and cleared at t = 0.2 s. The results are shown in Figure 12.

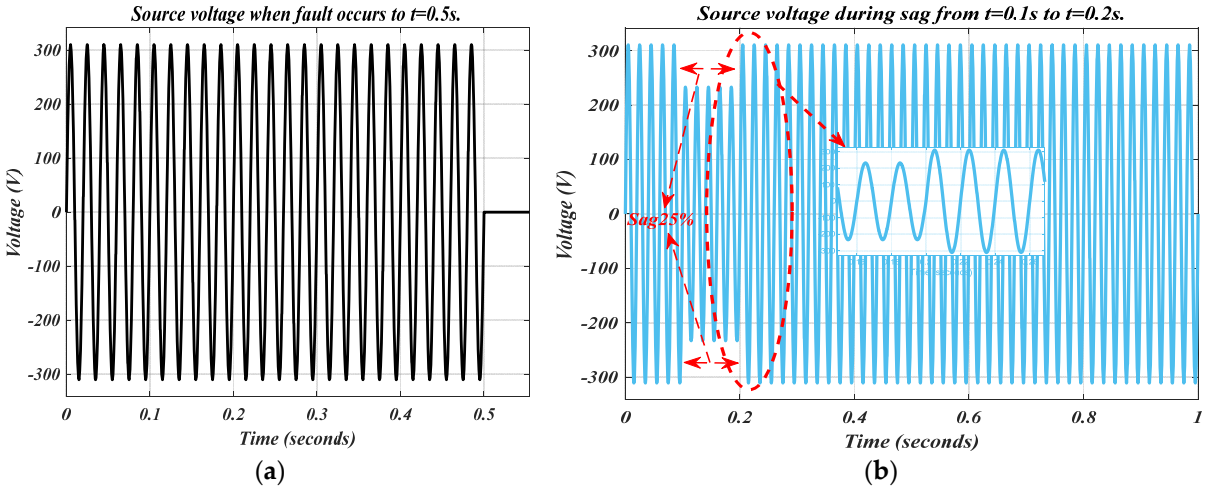

(**a**) (**b**)

Figure 12. Simulation results: (**a**) source voltage under faults; (**b**) source voltage during sag.

Figure 13 present the total harmonic distortion (THD), the grid current with active filtering has been reduced to 2.15%, which can be considered a significant enhancement.

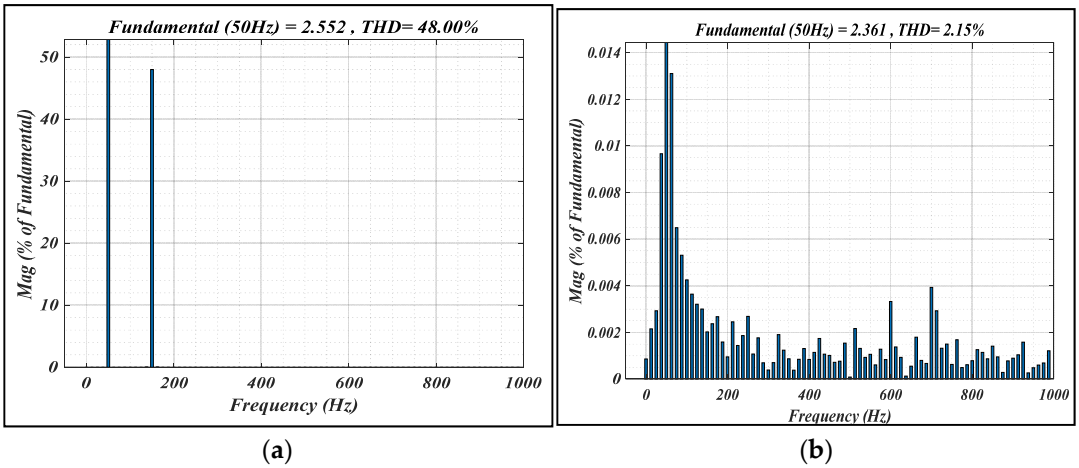

(**a**) (**b**)

Figure 13. Grid current THD analysis. (**a**) THD before active filtering; (**b**) THD after active filtering.

8. Experimental Results

The experimental setup designed to validate the proposed control strategy for the grid-connected PV system is shown in Figure 14. It consists of:

1. SEMIKRON IGBT based inverter;
2. Current and voltage sensors;
3. DC-DC boost converter;
4. Linear load;
5. dSPACE DS 1104 and power quality analyzer;
6. Host PC and oscilloscope;
7. Five PV panels.

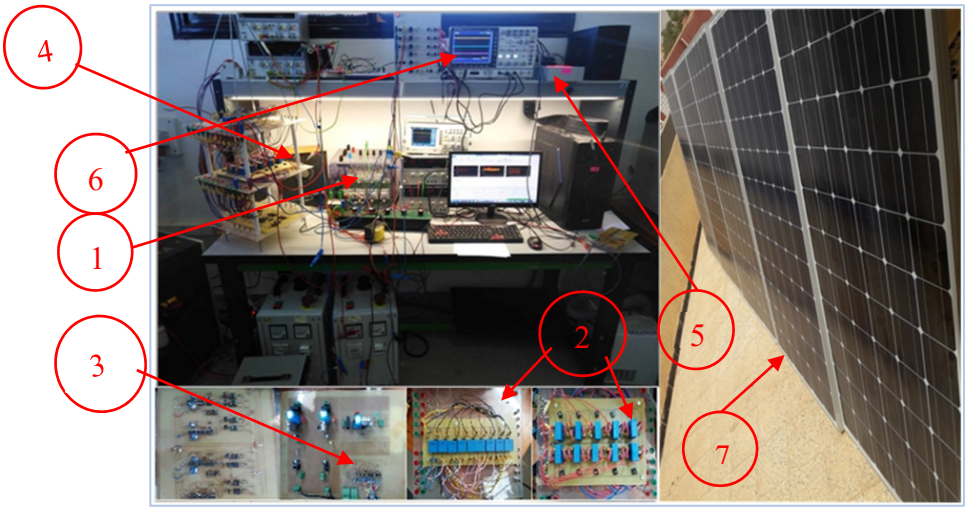

Figure 14. Experimental setup for the PV system.

Figure 15 shows the PV panel used in this work, with no load and in operating temperature conditions ranging from 25 °C to 35 °C; the solar irradiance is between 970 W/m^2 and 800 W/m^2.

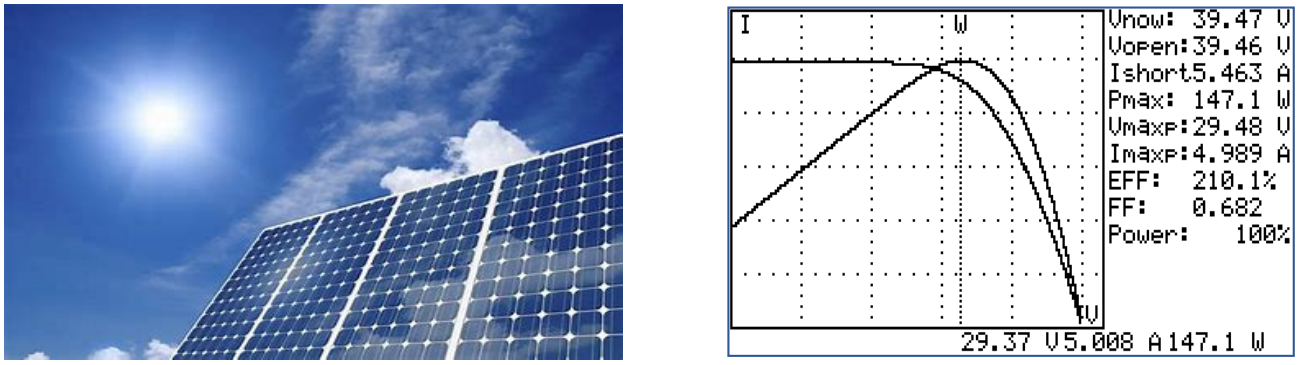

(**a**) (**b**)

Figure 15. Experimental tests: (**a**) irradiance conditions for the solar module; (**b**) solar panel I-V and P-V characteristics.

8.1. Islanding Mode

Initially, the boost converter and MPPT controller were designed and tested with linear and non-linear loads for an input voltage of around 200 V and an output voltage of 400 V. Figure 16a shows the experimental results of the PV voltage (185 V) and output voltage (330 V) of the boost converter. As shown in Figure 16b, the duty cycle has a value of 0.7.

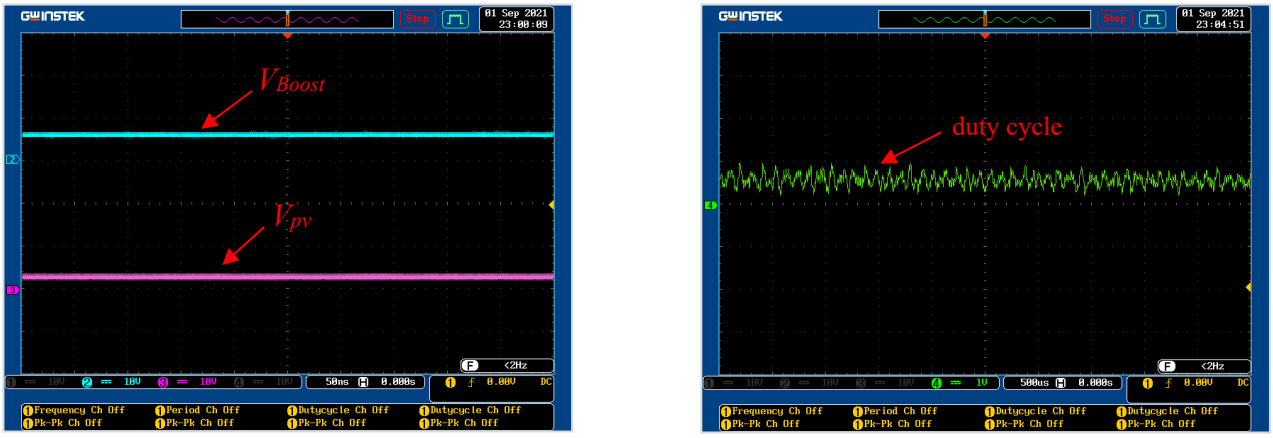

(**a**) (**b**)

Figure 16. Experimental results of (**a**) the PV voltage and output voltage of a boost converter, and (**b**) the duty cycle.

As can be seen in Figures 17 and 18, the converter reacts to the load by decreasing the current from 12.3 A to 5.65 A. The power remains constant at 1030 W for the input and output of the boost converter. This demonstrates that the proposed control system presents a good dynamic response in both grid-connected and islanded modes.

At time $t = 1$ s, the grid is disconnected, and the PV system is subjected to a fault that occurs at the PCC point. At this stage, it is necessary to satisfy the load demand by using the PV system in the islanded mode. The prime concern would be to disconnect the grid and use the available PV system power. Figures 19 and 20 are included to show, respectively, the voltage waveform during the fault and the active and reactive power supplied to both the linear and nonlinear loads.

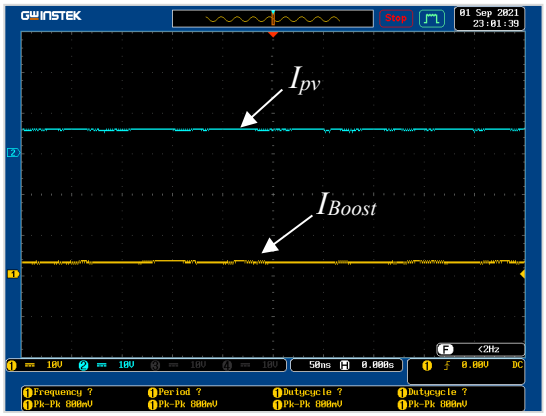

Figure 17. The PV and output currents of the boost converter.

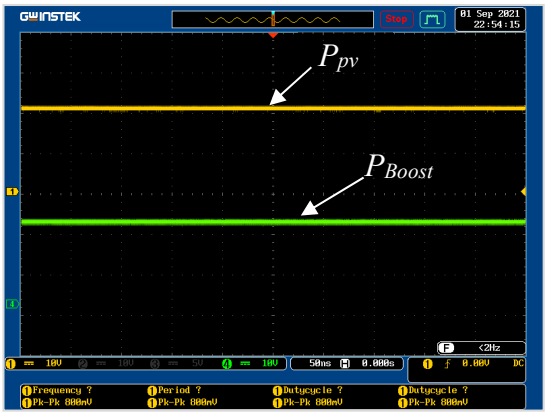

Figure 18. The input and output power of the boost converter.

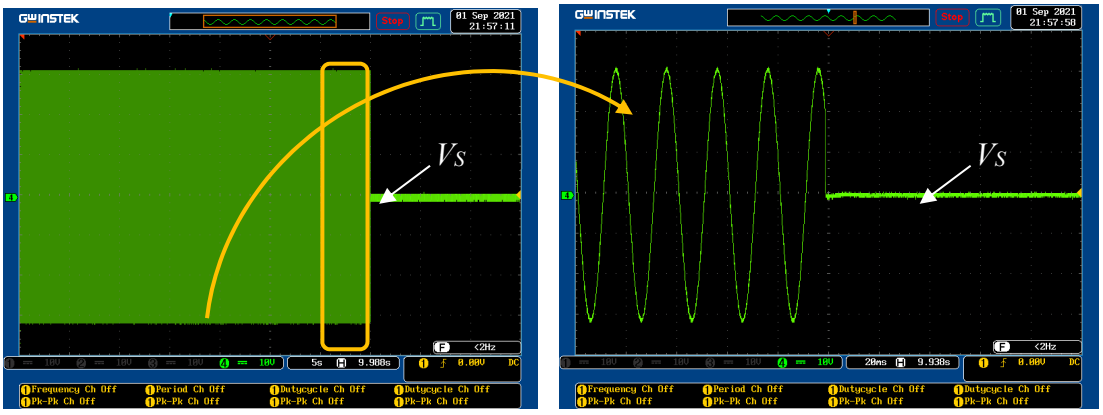

Figure 19. The source voltage waveform at the onset of the fault.

Moreover, and as can be seen in Figure 21a, the signals given to the gates of IGBTs 1 and 3 are in opposition to the signals delivered to the gates of IGBTs 2 and 4. Between the pulses delivered to the same branch of the inverter bridge, a dead time of 4 µs between the pulses has been maintained to prevent short circuits, as clearly seen in Figure 21b.

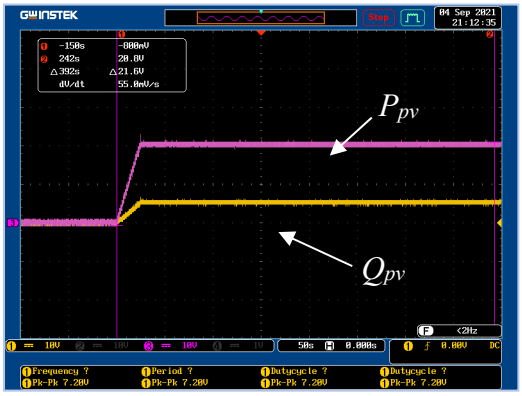

Figure 20. Active and reactive power supplied during islanding.

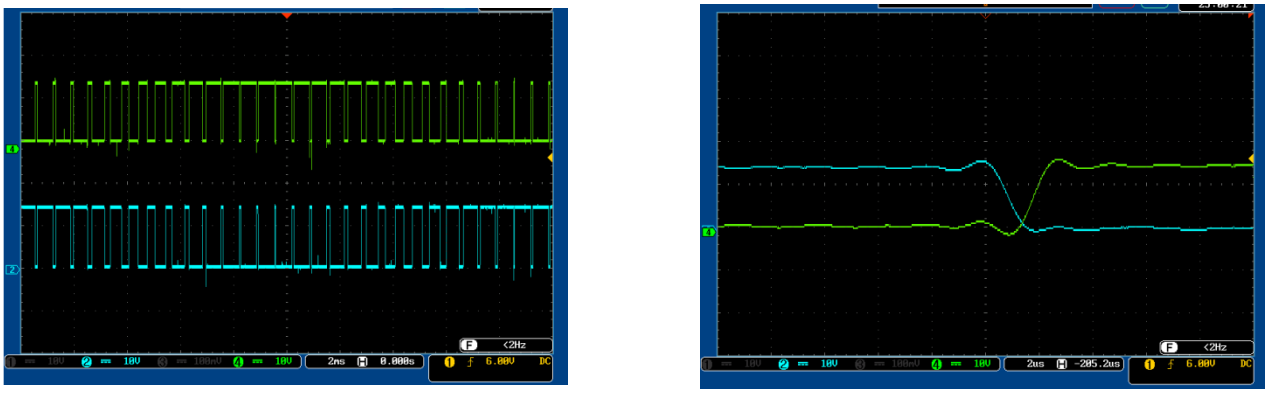

(**a**) (**b**)

Figure 21. (**a**) The control signal of the switches; (**b**) dead time for two control signals from two switches belonging to the same inverter arm.

8.2. Load Mode as Supplied Solely by the Grid

Figures 22 and 23 show the responses of the active and reactive powers supplied to the linear and non-linear loads, respectively. It can be seen that the value of the active power supplied to the linear load is 450 W, and that of the reactive power is equal to 125 Var. For the nonlinear load, the values of (P) and (Q) are 850 W and 210 Var, respectively. This clearly shows that the control system presents good dynamics.

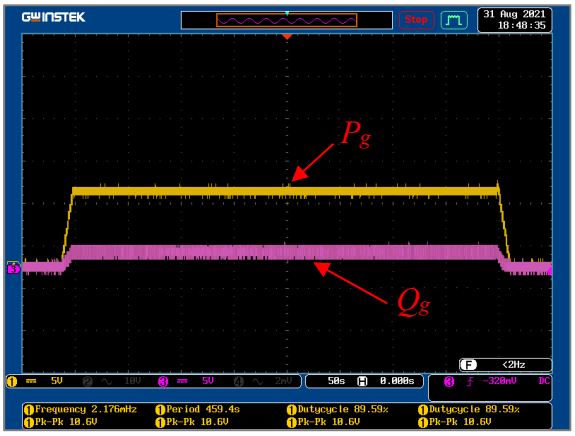

Figure 22. Experimental waveforms of the active and reactive power of a linear load.

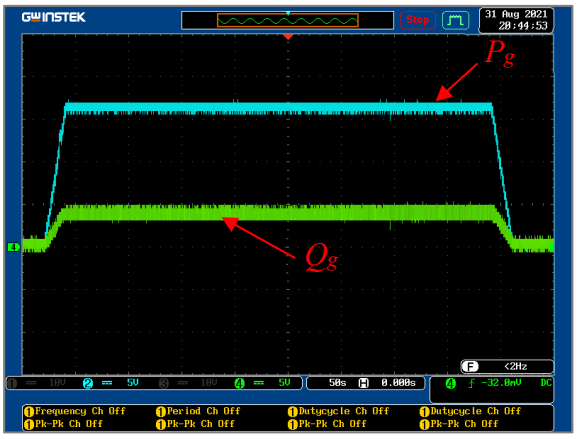

Figure 23. Experimental waveforms of the active and reactive power of a non-linear load.

8.3. Load Mode as Supplied by the Grid and PV System

When the experimental system is connected to the grid, the source begins to supply the load with sufficient power, as can be seen at the start of Figure 24, where the values of the active and reactive powers are equal to 850 W and 125 Var, respectively. When a fault occurs at the PCC point, the source fails to meet the load demand; hence, the PV system starts to supply power to the load. The corresponding results are clearly shown in Figure 24, where the values of P and Q become 1030 W and 210 Var, respectively.

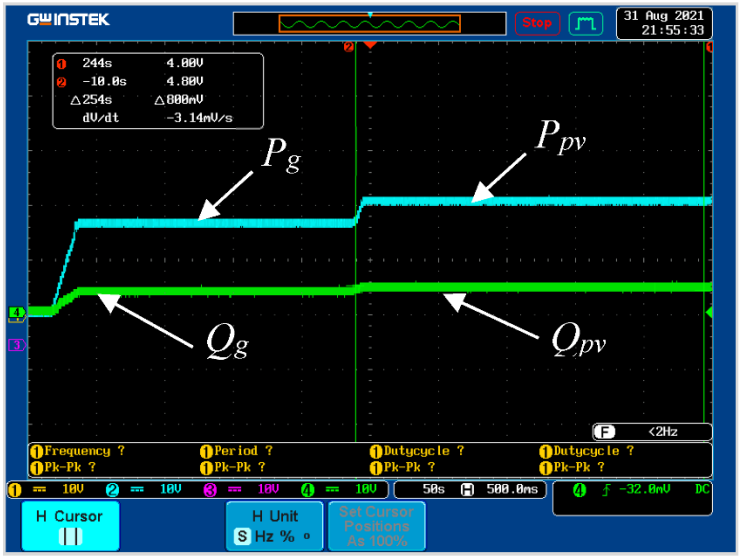

Figure 24. Experimental results of the load power from both the source and the PV system.

Figures 25 and 26 show the load current before and after harmonics correction.

The waveform of the load current before correcting the harmonics is presented in Figure 26. The spectral analysis indicates that the THD is 40.8%, as illustrated in Figure 27, where the load is supplied solely by the source. However, after the fault, the THD has reduced drastically to 2.8%, as can clearly be seen in Figure 28.

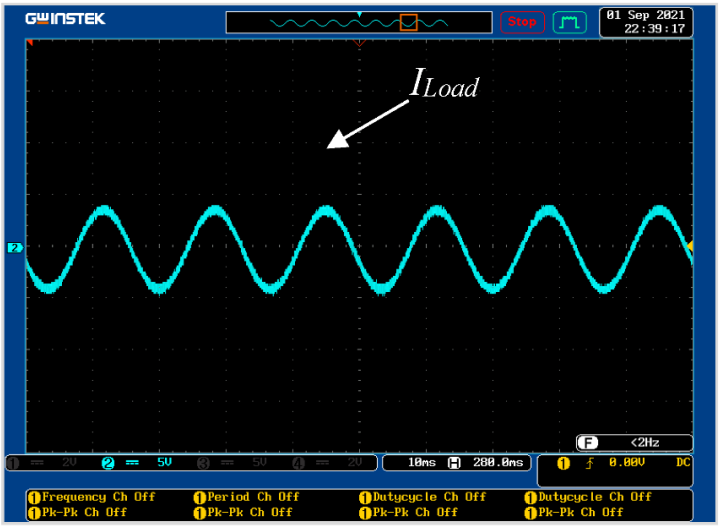

Figure 25. Experimental waveforms of the load current after correcting the harmonics.

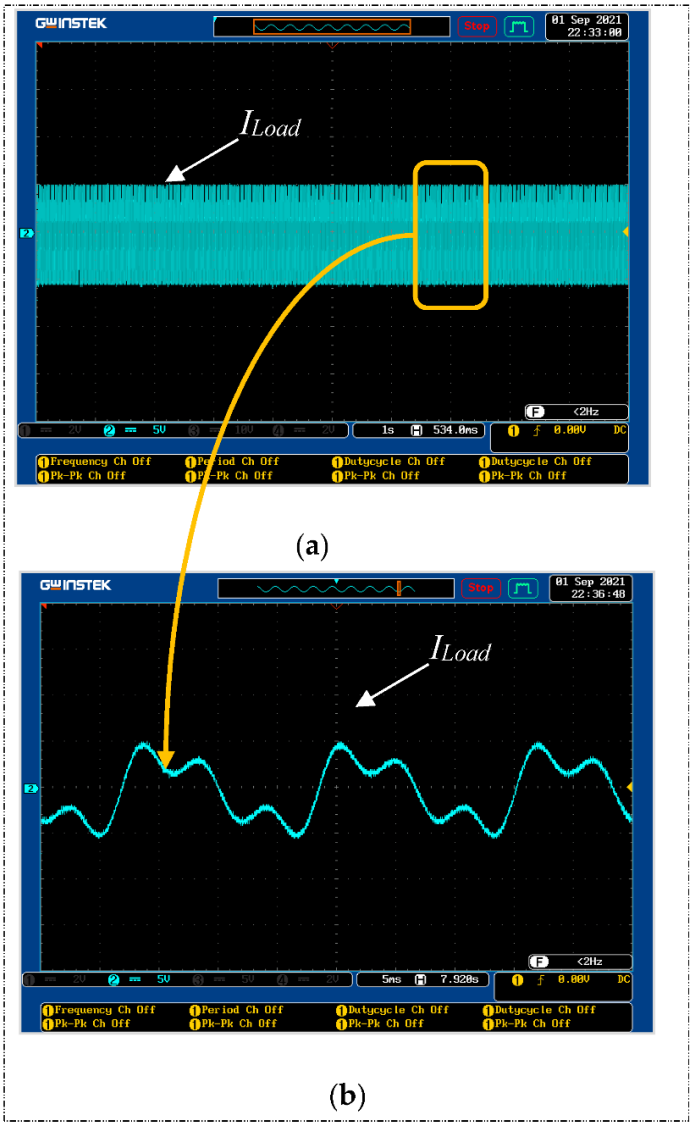

Figure 26. Experimental waveforms of the load current before correcting the harmonics. (**a**) Actual load current waveform; (**b**) Zooming of the load current.

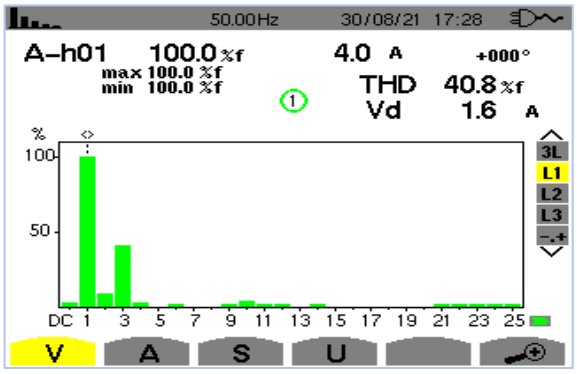

Figure 27. THD contents at the source supply only.

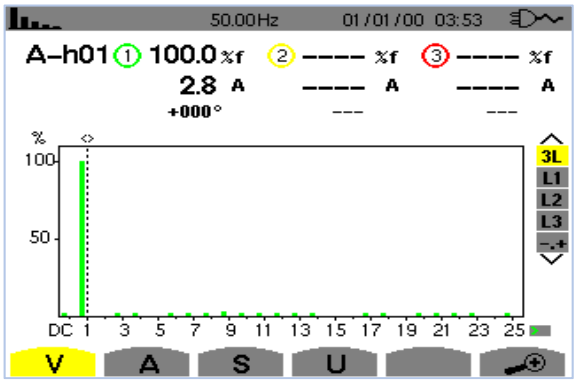

Figure 28. THD contents when the PV system is switched on.

8.4. Voltage Sag Mode

During the appearance of the voltage sag after the occurrence of a fault, the system is shifted to sag fault mode, and the current controller still supplies reactive current to restore the voltage according to the grid requirements, as shown in Figure 29.

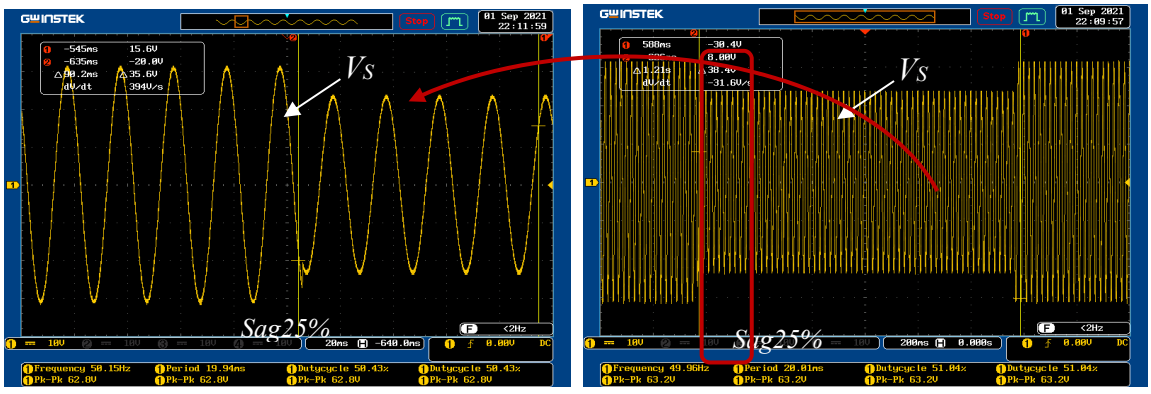

Figure 29. Source voltage during sag.

It is clear from Figure 30 that upon the occurrence of the sag, the load voltage remains unchanged, and the supply to the load is maintained by the PV system, due to the compensating current.

Both Figures 31 and 32 are included to show, respectively, the responses of the active and reactive powers during this sag disturbance and the DC link voltage across the capacitor, which is maintained to be constant at 330 V.

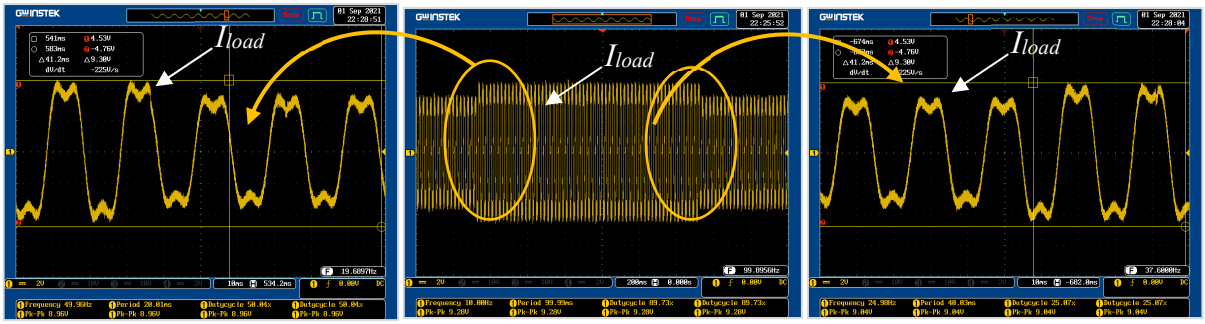

Figure 30. The current supplied by the current controller.

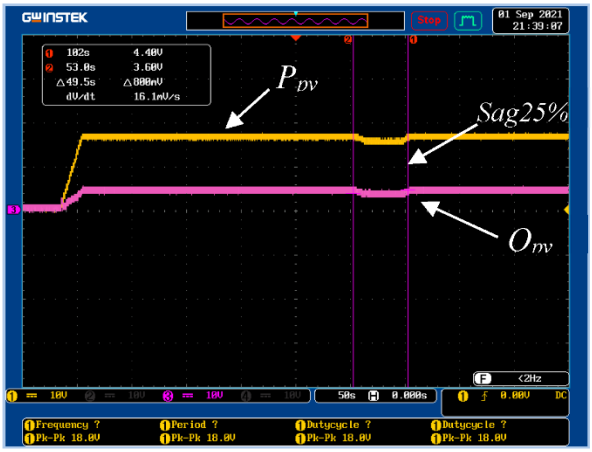

Figure 31. The response of the power waveforms during the voltage sag.

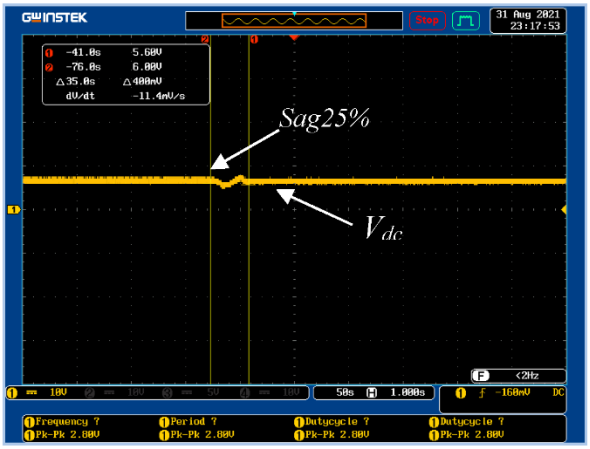

Figure 32. The response of the DC voltage waveform during the voltage sag.

We can see the close similarity of the simulated results with those of the experimental tests, as summarized below:

1. Waveforms of real and reactive power are depicted during islanding and during sag voltage, as shown by the simulated results in Figure 9 and those of the experimental test in Figure 20.
2. Waveforms of the DC link voltage and real and reactive power for a linear load are shown in the simulated results in Figure 10 and those of the experimental test in Figure 22.

3. Waveforms of the load supplied by the source and PV as well as the powers for linear and nonlinear loads are shown in the simulated results in Figure 11 and those of the experimental test in Figure 24.
4. Waveforms of the source voltage in fault conditions and during sag voltage are shown in the simulated results in Figure 12 and those of the experimental test in Figures 19 and 29.
5. Finally, the waveforms of the grid current THD analysis are shown in the simulated results in Figure 13 and those of the experimental test in Figures 27 and 28.

9. Conclusions

In this paper, a robust and effective control technique for a grid-connected single-phase photovoltaic (PV) system to improve the power quality at the PCC is proposed. The control strategy ensures that the PV inverter manages and performs its functions simultaneously (active power injection, reactive power compensation, and current harmonics filtering) without overrating by limiting its output current. Various scenarios, variable reactive power baselines, and nonlinear load power demands below and above PV power generation have been studied to assess the efficiency of the proposed strategy. Moreover, a performance analysis of the proposed control strategy when applied to a grid-connected inverter powered by PV has been carried out through simulations using MATLAB; some of the simulation results are included in this paper. The control scheme has been validated experimentally on a laboratory-scale PV system and tested under various grid fault and variable load conditions; the main results are included in this paper. The experimental results demonstrate that the proposed control strategy is robust, stable, and efficient. Moreover, in this research, the proposed controller was able to successfully deal with both linear and nonlinear load conditions and demonstrates that the use of the PV system significantly enhances the power quality.

Referencing several studies that have been reviewed, Table 2 summarizes the previous research work investigating different control techniques for grid-connected PV systems, with a brief outline of their merits and disadvantages.

Table 2. Summary of the research work related to grid-connected PV system control strategies.

Ref.	Year	Method	Merits/Disadvantages
[41]	2017	Conventional PQ control method	- Ease of implementing the PI controller - Response is within an acceptable range
[42]	2015	CMPN-based PI controller	- Quick response - Reduced oscillations in power waveforms - Optimum active current is injected during fault time
[43]	2016	Resonant controller	- Reduced oscillations in DC link voltage - High over current conditions
[34]	2014	Dynamic resistor braking	- Ease of implementation - No reactive current injection
[35]	2016	Quasi Z-source inverter	- Regulation of DC link voltage - Reactive power is not considered
[44]	2015	Energy storage system in supercapacitor	- Ease of design and implementation - Oscillations in power observed
[36]	2019	Conventional PI-based PQ control	- Easy to design and implement - Transfer of maximum active power into the grid during faults
[40]	2018	Model predictive control approach	- Does not support over current reduction in the grid - Quick response time
[45]	2017	Fault ride in control based on fuzzy logic	- Response is rapid and hardware implementation is easy - High over current conditions
[46]	2015	Probabilistic wavelet fuzzy-based neural network controller	- Requires complex calculation - High over current conditions

Author Contributions: Methodology, A.B. and M.B.S.; Software, A.B.; Validation, A.D.; Formal analysis, A.D. and A.A.; Investigation, A.A. and M.B.S.; Resources, A.D., T.T. and O.A.; Data curation, A.D. and O.A.; Writing—original draft, A.D., T.T. and O.A.; Writing—review & editing, M.D. and M.B.S.; Supervision, M.D. and M.B.S.; Project administration, M.B.S.; Funding acquisition, A.D. All authors have read and agreed to the published version of the manuscript.

Funding: This research received no external funding.

Data Availability Statement: Not applicable.

Acknowledgments: This project was funded by the Deanship of Scientific Research (DSR) at the Islamic University of Madinah (IUM) in Saudi Arabia, under the Institutional Finance Program "Tamayyuz 2" via Grant No. 656 in November 2020. The authors, therefore, acknowledge with gratitude the support of DSR in IUM and wish to extend their appreciation for the full financial and moral support received.

Conflicts of Interest: The authors declare that there is no conflict of interest.

Abbreviations

PV	Photovoltaic
PWM	Pulse width modulation
MPPT	Maximum power point tracking
ANFIS	Adaptive neuro-fuzzy inference
OSG	Orthogonal signal generator
THD	Total harmonic distortion
PCC	Point of common coupling
PQ	Power quality
PLL	phase-locked loops
LP	Low pass filter
FRT	Fault ride-through
P&O	Perturb and observe
I_{PV}, V_{PV}	PV array current and voltage
I_{gE}, I_{gF} and V_{gE}, V_{gF}	Grid current and voltage
P Q	The real and reactive powers
h	Harmonic order
ω_0	Fundamental frequency
T_s	Sampling period
P_{MPP}	PV array MPP power
N	strings of PV

Appendix A

The proposed system uses the ANFIS system, with E and CE as the inputs and y as the output. The fuzzy IF-THEN rules are implemented as follows in ANFIS:

Rule1:
IF 'E' is E_1 and 'CE' is EC_1 Then $y = a_1E + b_1CE + c_1$
Rule1:
IF 'E' is E_2 and 'CE' is EC_2 Then $y = a_2E + b_2CE + c_2$

In Figure 6, the ANFIS controller's Takagi–Sugeno model-based design on five layers is shown. The function of each layer is given below:

L1: This layer receives the inputs and converts them to fuzzy sets. Each node '*i*' has a function that allows it to be flexible.

$$O_{1,I} = \mu_{Mi}(E) \text{ for } i = 1, 2 \tag{A1}$$

$$O_{1,I} = \mu_{Ni-2}(E) \text{ for } i = 3, 4 \tag{A2}$$

The inputs are E and CE, and the linguistic labels are Mi and Ni-2. The triangle MFs are utilized and the resulting MFs once training is finished are displayed in Figure 10.

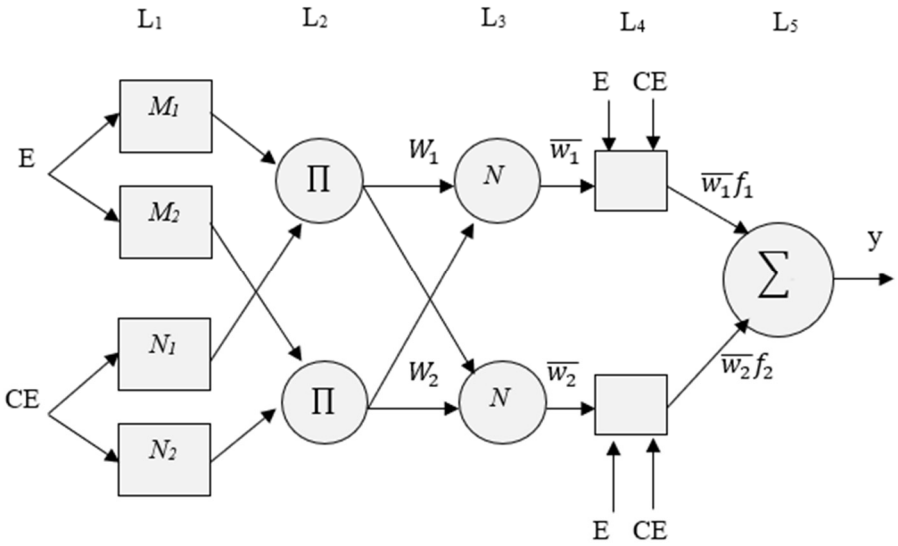

Figure A1. The architecture of ANFIS.

L2: The multiplication of all incoming signals is one of this layer's outputs. This layer's nodes are all static π nodes.

$$O_{2,I} = w_i = \mu_{Mi}(\mathrm{E})\mu_{Ni}(\mathrm{CE}) \tag{A3}$$

The rule firing strength is represented by a node output. The fuzzy AND is used as a function.

L3: Normalization of the rules is calculated in this layer. It is the ratio of the firing strength of each rule to the total value of the firing strengths. The nodes are labeled N and are static.

$$O_{3,\,i} = \overline{w_i} = \frac{w_i}{w_1 + w_2} \quad i = 1, 2, \ldots \tag{A4}$$

L4: This is the defuzzification layer, where the nodes are versatile by a function.

Here, $\overline{w_i}$ is the normalized firing strength and the values of a_1, b_1, and c_1 are the subsequent parameters.

L5: This contains a static node, labeled Σ, which will add together all incoming signals to calculate the output.

$$O_{5,i} = y = \sum \overline{w_i} f_i = \frac{\sum w_i f_i}{\sum w_i} \tag{A5}$$

All outputs were set to zero before the ANFIS system began training. Following the completion of training, the ANFIS system produced output values, which are listed in Table A1. The ANFIS system was educated using the MATLAB platform's hybrid learning method. The various datasets seen in the experimental results using the traditional controller were used to train the ANFIS system to enhance its performance. Figure 11 depicts the ANFIS controller's surface view. In a three-dimensional perspective, it displays the connection between two inputs and outputs. It aids in comprehending the controller output's performance as a function of the inputs.

Table A1. Training parameter values for the ANFIS system.

Nomenclature	Value
TDPs	350,000
CDP	60,000
MF	7
Nodal points	131
NP	42
LP	49
TP	91
FR	49
NE	150

Appendix B

Table A2. Output values of the ANFIS system.

CE E	EC_1	EC_2	EC_3	EC_4	EC_5	EC_6	EC_7
E_1	−0.5	−0.3	−0.0030	0	0	0	0
E_2	−0.35	−0.14	0.07	0	0	0	0
E_3	0	0.07	0.28	0.42	−0.02	0	0
E_4	0	0	0.5	0.7	0.5	−0.06	0
E_5	0	0	0	1.2	0.9	1.06	0.01
E_6	0	0	0	0	0.9	0.9	1.3
E_7	0	1.1	0.6	0	0	0.6	0.9

Appendix C

Details of the Simulink implementation of a single-phase grid-connected PV system with an LCL filter, as depicted in Figure A2.

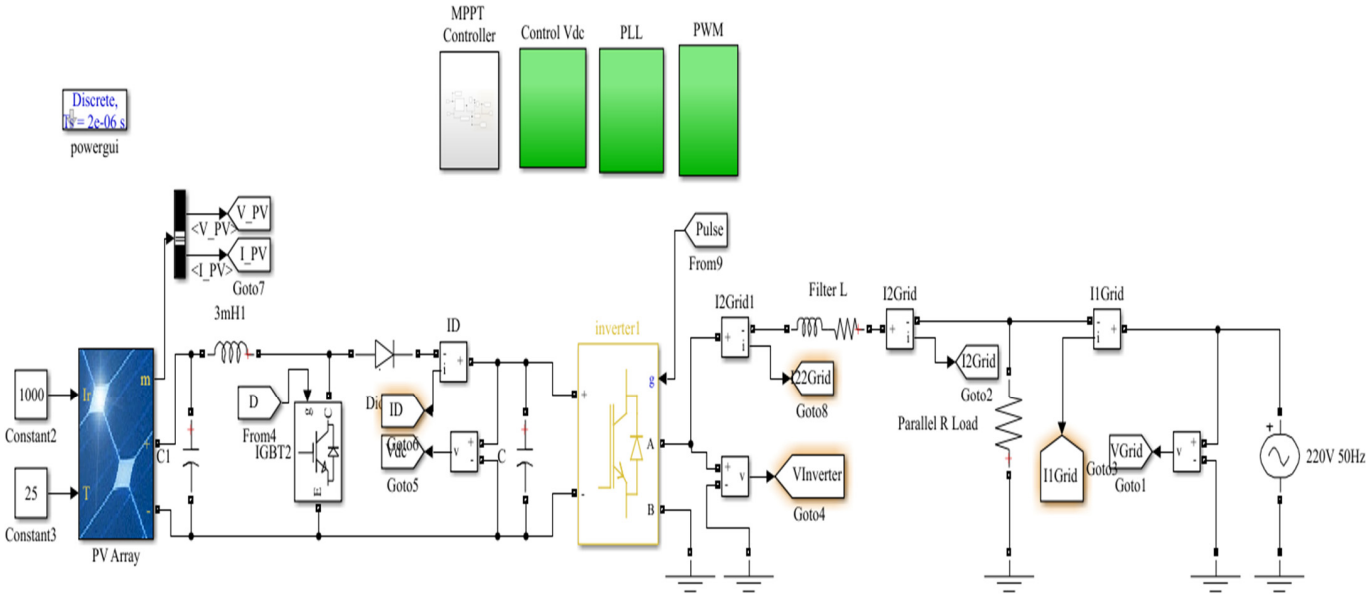

Figure A2. Simulink model of the single-phase grid-connected PV system.

References

1. Dugan, R.C.; Mc Granaghan, M.F.; Beaty, H.W. *Electrical Power Systems Quality*; McGraw-Hill: New York, NY, USA, 1996.
2. Farhadi-Kangarlu, M.; Babaei, E.; Blaabjerg, F. A comprehensive review of dynamic voltage restorers. *Int. J. Electr. Power Energy Syst.* **2017**, *92*, 136–155. [CrossRef]
3. Sankaren, C. *Power Quality*; CRC Press: Boca Raton, FL, USA, 2017.
4. *IEEE Std. 1346-1998*; IEEE Recommended Practice for Evaluating Electric Power System Compatibility with Electronic Process Equipment. IEEE: Piscataway, NJ, USA, 1998.
5. *IEC Std. 61000-2-1*; Electromagnetic Compatibility (EMC), Part 2: Environment, Section 1: Description of the Environment, Electromagnetic Environment for Low-Frequency Conducted Disturbances and Signaling in Public Power Supply Systems. IEC: Geneva, Switzerland, 1990.
6. Rauf, A.M.; Khadkikar, V. Integrated photovoltaic and dynamic voltage restorer system configuration. *IEEE Trans. Sustain. Energy* **2015**, *6*, 400–410. [CrossRef]
7. Kusko, A. *Power Quality in Electrical Systems*; McGraw-Hill Education: New York, NY, USA, 2007.
8. Gotekar, P.S.; Muley, S.P.; Kothari, D.P. A Single Phase Grid Connected PV System working in Different Modes. *Eng. Technol. Appl. Sci. Res.* **2020**, *10*, 6374–6379. [CrossRef]
9. Proceedings of the 27th Conference of the Parties to the United Nations Framework Convention on Climate Change, COP27, Sharm el-Sheikh, Egypt, 6–20 November 2022; Available online: https://www.un.org/en/climatechange/cop27 (accessed on 8 May 2023).
10. Shukhobodskiy, A.A.; Colantuono, G. RED WoLF: Combining a battery and thermal energy reservoirs as a hybrid storage system. *Appl. Energy* **2020**, *274*, 115209. [CrossRef]
11. Toosi, H.A.; Del Pero, C.; Leonforte, F.; Lavagna, M.; Aste, N. Machine learning for performance prediction in smart buildings: Photovoltaic self-consumption and life cycle cost optimization. *Appl. Energy* **2023**, *334*, 120648. [CrossRef]
12. Teodorescu, R.; Liserre, M.; Rodríguez, P. *Grid Converters for Photovoltaic and Wind Power Systems*; John Wiley & Sons: Chichester, UK, 2011.
13. Mahamudul, H.; Saad, M.; Henk, M.I. Photovoltaic system modeling with fuzzy logic based maximum power point tracking algorithm. *Int. J. Photoenergy* **2013**, *2013*, 762946. [CrossRef]
14. Sangwongwanich, A.; Blaabjerg, F. Mitigation of interharmonics in PV systems with maximum power point tracking modification. *IEEE Trans. Power Electron.* **2019**, *34*, 8279–8282. [CrossRef]
15. Gotekar, P.S.; Muley, S.P.; Kothari, D.P. Fuzzy Inference based control of single phase grid connected photovoltaic system. In Proceedings of the 2019 Innovations in Power and Advanced Computing Technologies (i-PACT), Vellore, India, 22–23 March 2019; pp. 1–3.
16. Vosoughi, N.; Hosseini, S.H.; Sabahi, M. Single-phase common-grounded transformer-less grid-tied inverter for PV application. *IET Power Electron.* **2020**, *13*, 157–167. [CrossRef]
17. Ghosh, S.S.; Nathan, K.S.; Siwakoti, Y.P.; Long, T. Dual polarity DC–DC converter integrated grid-tied single-phase transformer less inverter for solar application. *J. Eng.* **2019**, *2019*, 3962–3966. [CrossRef]
18. Datta, A.; Sarker, R.; Hazarika, I. An efficient technique using modified p–q theory for controlling power flow in a single-stage single-phase grid-connected PV system. *IEEE Trans. Ind. Inform.* **2018**, *15*, 4635–4645. [CrossRef]
19. Anurag, A.; Yang, Y.; Blaabjerg, F. Thermal performance and reliability analysis of single-phase PV inverters with reactive power injection outside feed-in operating hours. *IEEE J. Emerg. Sel. Top. Power Electron.* **2015**, *3*, 870–880. [CrossRef]
20. Yang, Y.; Wang, H.; Blaabjerg, F. Reactive power injection strategies for single-phase photovoltaic systems considering grid requirements. *IEEE Trans. Ind. Appl.* **2014**, *50*, 4065–4076. [CrossRef]
21. Yang, Y.; Blaabjerg, F.; Zou, Z. Benchmarking of grid fault modes in single-phase grid-connected photovoltaic systems. *IEEE Trans. Ind. Appl.* **2013**, *49*, 2167–2176. [CrossRef]
22. Yang, Y.; Blaabjerg, F. Low-voltage ride-through capability of a single-stage single-phase photovoltaic system connected to the low-voltage grid. *Int. J. Photoenergy* **2013**, *2013*, 257487. [CrossRef]
23. Ikken, N.; Bouknadel, A.; Haddou, A.; Tariba, N.-E.; El Omari, H.; El Omari, H. PLL synchronization method based on second-order generalized integrator for single phase grid connected inverters systems during grid abnormalities. In Proceedings of the 2019 International Conference on Wireless Technologies, Embedded and Intelligent Systems (WITS), Fez, Morocco, 3–4 April 2019; pp. 1–5.
24. Butt, H.Z.; Awon, M.; Khalid, H.A. Performance Analysis of a Continuous and Discretized Second Order Generalized Integrator based Phase Lock Loop for Single Phase Grid Connected PV Systems. In Proceedings of the 2018 International Conference on Power Generation Systems and Renewable Energy Technologies (PGSRET), Islamabad, Pakistan, 10–12 September 2018; pp. 1–6.
25. Panda, A.K.; Patnaik, N. Combined operation of a new power angle control unit vector template based unified power quality conditioner and fuel cell stack supply with effective utilization of shunt and series inverter. *Electr. Power Compon. Syst.* **2016**, *44*, 2048–2058. [CrossRef]
26. Nouaiti, A.; Mesbahi, A.; Saad, A.; Khafallah, M.; Reddak, M. Realization of a Single-Phase Multilevel Inverter for Grid-Connected Photovoltaic System. *Eng. Technol. Appl. Sci. Res.* **2018**, *8*, 3344–3349. [CrossRef]
27. Krithiga, S.; Gounden, N.G.A. Power electronic configuration for the operation of PV system in combined grid-connected and stand-alone modes. *IET Power Electron.* **2014**, *7*, 640–647. [CrossRef]

28. Subudhi, P.S.; Krithiga, S. PV and grid interfaced plug-in EV battery charger operating in P-VG PV and VG modes. *Int. J. Recent Technol. Eng.* **2019**, *8*, 3431–3443. [CrossRef]
29. Reddy, V.R.; Sreeraj, E.S. A feedback-based passive islanding detection technique for one-cycle-controlled single-phase inverter used in photovoltaic systems. *IEEE Trans. Ind. Electron.* **2019**, *67*, 6541–6549. [CrossRef]
30. Raza, S.A.; Jiang, J. A benchmark distribution system for investigation of residential microgrids with multiple local generation and storage devices. *IEEE Open Access J. Power Energy* **2019**, *7*, 41–50. [CrossRef]
31. Lam, L.H.; Phuc, T.D.H.; Hieu, N.H. Simulation models for three-phase grid connected PV inverters enabling current limitation under unbalanced faults. *Eng. Technol. Appl. Sci. Res.* **2020**, *10*, 5396–5401. [CrossRef]
32. Jamil, M.; Rizwan, M.; Kothari, D.P. *Grid Integration of Solar Photovoltaic Systems*; CRC Press: Boca Raton, FL, USA, 2017.
33. Kazmierkowski, M.P. Renewable Energy Devices and Systems with Simulations in MATLAB and ANSYS [Book News]. *IEEE Ind. Electron. Mag.* **2018**, *12*, 80–83. [CrossRef]
34. Hasanien, H.M. An adaptive control strategy for low voltage ride through capability enhancement of grid-connected photovoltaic power plants. *IEEE Trans. Power Syst.* **2015**, *31*, 3230–3237. [CrossRef]
35. Cárdenas, R.; Díaz, M.; Rojas, F.; Clare, J.; Wheeler, P. Resonant control system for low-voltage ride-through in wind energy conversion systems. *IET Power Electron.* **2016**, *9*, 1297–1305. [CrossRef]
36. Ben Abdelkader, A.; Toumi, T.; Abdelkhalek, O. Experimental verification of dynamic voltage restorer fed by solar PV: Lithium-ion battery storage for lasting power quality improvement. *Electr. Eng.* **2022**, *104*, 4581–4593. [CrossRef]
37. Hossain, M.K.; Ali, M.H. Fuzzy logic controlled power balancing for low voltage ride-through capability enhancement of large-scale grid-connected PV plants. In Proceedings of the 2017 IEEE Texas Power and Energy Conference (TPEC), College Station, TX, USA, 9–10 February 2017; pp. 1–6.
38. Lin, F.-J.; Lu, K.-C.; Ke, T.-H.; Yang, B.-H.; Chang, Y.-R. Reactive power control of three-phase grid-connected PV system during grid faults using Takagi–Sugeno–Kang probabilistic fuzzy neural network control. *IEEE Trans. Ind. Electron.* **2015**, *62*, 5516–5528. [CrossRef]
39. Toumi, T.; Allali, A.; Meftouhi, A.; Abdelkhalek, O.; Benabdelkader, A.; Denai, M. Robust control of series active power filters for power quality enhancement in distribution grids: Simulation and experimental validation. *ISA Trans.* **2020**, *107*, 350–359. [CrossRef]
40. Al-Durra, A.; Fayyad, Y.; Muyeen, S.; Blaabjerg, F. Fault ride-through of a grid-connected photovoltaic system with quasi Z source inverter. *Electr. Power Compon. Syst.* **2016**, *44*, 1786–1800. [CrossRef]
41. Bae, Y.; Vu, T.-K.; Kim, R.-Y. Implemental control strategy for grid stabilization of grid-connected PV system based on German grid code in symmetrical low-to-medium voltage network. *IEEE Trans. Energy Convers.* **2013**, *28*, 619–631. [CrossRef]
42. Blaabjerg, F.; Teodorescu, R.; Liserre, M.; Timbus, A.V. Overview of control and grid synchronization for distributed power generation systems. *IEEE Trans. Ind. Electron.* **2006**, *53*, 1398–1409. [CrossRef]
43. Hasaneen, M.M.; Badr, M.A.; Atallah, A.M. Control of active/reactive power and low-voltage ride through for 40 kW three-phase grid-connected single-stage PV system. *CIRED-Open Access Proc. J.* **2017**, *2017*, 1655–1659. [CrossRef]
44. Hossain, M.K.; Ali, M.H. Low voltage ride through capability enhancement of grid connected PV system by SDBR. In Proceedings of the 2014 IEEE PES T&D Conference and Exposition, Medellin, Colombia, 10–13 September 2014; pp. 1–5.
45. Worku, M.Y.; Abido, M.A. Grid-connected PV array with supercapacitor energy storage system for fault ride through. In Proceedings of the 2015 IEEE International Conference on Industrial Technology (ICIT), Seville, Spain, 17–19 March 2015; pp. 2901–2906.
46. Bighash, E.Z.; Sadeghzadeh, S.M.; Ebrahimzadeh, E.; Blaabjerg, F. Improving performance of LVRT capability in single-phase grid-tied PV inverters by a model-predictive controller. *Int. J. Electr. Power Energy Syst.* **2018**, *98*, 176–188. [CrossRef]